



Influence of Ridge Spacing, Ridge Width, and Reynolds Number on Secondary Currents in Turbulent Channel Flow Over Triangular Ridges

Oleksandr Zhdanov¹ · Thomas O. Jelly^{1,2} · Angela Busse¹

Received: 30 April 2023 / Accepted: 4 September 2023 / Published online: 26 September 2023
© The Author(s) 2023

Abstract

Most studies of secondary currents (SCs) over streamwise aligned ridges have been performed for rectangular ridge cross-sections. In this study, secondary currents above triangular ridges are systematically studied using direct numerical simulations of turbulent channel flow. The influence of ridge spacing on flow topology, mean flow, and turbulence statistics is investigated at two friction Reynolds numbers, 550 and 1000. In addition, the effects of ridge width on SCs, which have not previously been considered for this ridge shape, are explored. The influence of SCs on shear stress statistics increases with increased ridge spacing until SCs fill the entire channel. One of the primary findings is that, for ridge configurations with pronounced secondary currents, shear stress statistics exhibit clear Reynolds number sensitivity with a significant growth of dispersive shear stress levels with Reynolds number. In contrast to rectangular ridges, no above-ridge tertiary flows are observed for the tested range of ridge widths. Flow visualisations of SCs reveal the existence of corner vortices that form at the intersection of the lateral ridge sides and the smooth-wall sections. These are found to gradually disappear as ridges increase in width. Premultiplied spectra of streamwise velocity fluctuations show strong dependency on the spanwise sampling location. Whereas spanwise averaged spectra show no strong modifications by SCs, a significant increase of energy levels emerges at higher wavelengths for spectra sampled at the spanwise locations that correspond to the centres of the secondary currents.

Keywords Secondary currents · Ridge-type roughness · DNS · Turbulent channel flow

✉ Oleksandr Zhdanov
oleksandr.zhdanov@glasgow.ac.uk

Thomas O. Jelly
tom.jelly@unimelb.edu.au

Angela Busse
angela.busse@glasgow.ac.uk

¹ James Watt School of Engineering, University of Glasgow, Scotland G12 8QQ, UK

² Department of Mechanical Engineering, University of Melbourne, Melbourne, VIC 3010, Australia

1 Introduction

Secondary currents (SCs) occur in a wide range of wall-bounded flow configurations, where their time-mean signature manifests itself as streamwise vortices in the cross-plane perpendicular to the primary flow direction. Based on their generation mechanism SCs were classified by Prandtl into two kinds (Prandtl 1952). Secondary currents of the first kind are formed as a result of the mean flow curvature, for example, as Dean vortices in flows through pipe bends, while secondary currents of the second kind are a result of turbulence anisotropy and gradients of turbulent stresses. For the latter kind, a well-known example is the flow through non-circular ducts (Nikuradse 1930), where SCs form in the corners of the duct. Experiments by Hinze (1967, 1973), where strips of roughness were applied to one wall of a rectangular channel, showed that surfaces with spanwise heterogeneity can also generate SCs. In these experiments secondary currents formed not only in the channel corners but also at the edges of the roughness strips. These currents also originate from turbulence anisotropy and spatial gradients of the Reynolds stresses and therefore fall under Prandtl's secondary flows of the second kind (Anderson et al. 2015). Despite being relatively weak compared to the mean flow (e.g., Kevin et al. 2017), SCs can have a significant impact on the mean flow profile and turbulence statistics. In particular, the presence of secondary currents induces elevated levels of dispersive stresses not only close to the wall as in case of typical rough surfaces with short correlation lengths but also in the outer layer (Vanderwel et al. 2019).

Systematic studies usually distinguish between two types of spanwise heterogeneous surfaces that induce secondary currents: ridge-type roughness and strip-type roughness (Wang and Cheng 2006). The former type includes surfaces with spanwise variation of topography, i.e., variation of local elevation, while the latter type covers surfaces with spanwise variation of skin friction. In both cases, the streamwise vortices that represent the SCs are separated by high- and low-momentum pathways (HMPs and LMPs), which correspond to the downwash and upwash flow regions, respectively, alternating in the spanwise direction. Ridge-type and strip-type roughness have been studied experimentally and numerically for several canonical wall-bounded configurations such as zero pressure gradient turbulent boundary layers (Vanderwel and Ganapathisubramani 2015; Hwang and Lee 2018; Wangsawijaya et al. 2020), closed channels (Chung et al. 2018; Stroh et al. 2020a), open channels (Stroh et al. 2020b; Zampiron et al. 2020), and pipe flow (Chan et al. 2018; Liu et al. 2022).

Surfaces with spanwise variation of roughness topography are also investigated in the context of riblets (e.g., Bechert et al. 1997; García-Mayoral and Jiménez 2011). However, while sharing geometric similarity with ridge-type roughness, riblets and ridges interact with the flow on different scales. In case of riblets, their size and effects are related to the inner scale of wall-bounded turbulence and investigations of flow over riblets mainly consider their drag-reducing or drag-increasing properties (e.g., Endrikat et al. 2021; Von Deyn et al. 2022). In addition, due to the small size of riblets with respect to the outer scale of the flow, especially at typical Reynolds numbers for the applications of riblets for drag reduction, they are not expected to induce large-scale secondary flows. In contrast, investigations of ridge-type roughness concentrate on their ability to generate large-scale secondary currents which emerge at spanwise ridge spacings of the order of the outer scale of the flow, i.e., the channel half-height or boundary layer thickness. Therefore, we will focus in the following on studies investigating ridge-type surfaces that generate macroscopic secondary currents.

For ridge-type roughness, which is the subject of the present study, most systematic investigations have been performed using ridges with rectangular cross-section (Vanderwel and Ganapathisubramani 2015; Hwang and Lee 2018; Vanderwel et al. 2019; Medjnoun et al. 2020). Spacing between adjacent ridges was found to be one of the primary parameters that characterises spanwise heterogeneity of the surface and has a strong effect on the size and strength of SCs (Vanderwel and Ganapathisubramani 2015; Hwang and Lee 2018). For rectangular ridges Vanderwel and Ganapathisubramani (2015) determined that a ridge spacing of approximately 50% of the outer scale of the flow is required to induce significant SCs. As the ridges are placed further apart, secondary currents increase in size and eventually become space-filling and their strength is maximised when the ridge spacing reaches the outer length scale of the flow (Vanderwel and Ganapathisubramani 2015). Further increase in ridge spacing leads to emergence of tertiary flows which are formed in the centre of the valleys in between ridges (see, e.g., Vanderwel and Ganapathisubramani 2015; Hwang and Lee 2018). Similarly to secondary currents, tertiary flows are represented by a pair of counter-rotating streamwise vortices although of reduced strength compared to SCs, e.g., Vanderwel and Ganapathisubramani (2015) reported a difference in strength of approximately 50%.

Another important parameter that influences secondary currents over rectangular ridges is the ridge width. The increase of ridge width was found to have an opposite effect on the strength of SCs compared to the ridge spacing: at constant spacing in terms of the outer scale of the flow wider ridges produce weaker secondary currents (Hwang and Lee 2018; Medjnoun et al. 2020). However, both parameters share commonalities when considering their effect on flow topology. Wide rectangular ridges also generate pronounced tertiary flows, but instead of emerging at the centre of the valley between ridges, as for wide ridge spacing, they form above the ridge crest. Technically, these flow structures can also be classified as “secondary currents” based on Prandtl’s definition but are widely referred to as “tertiary flows” to distinguish between secondary currents generated by the sides of the ridges and the additional persistent streamwise vortices that emerge over wide ridges. For very wide ridges, an additional downwash region forms at the centre of the ridge. These phenomena are observed for rectangular ridges whose width exceeds approximately half of the outer scale of the flow (Hwang and Lee 2018; Medjnoun et al. 2020). However, this is a result of formation of the tertiary structures and upwash regions associated with SCs are still tied to the ridge sides and no reversal in their rotational direction is observed.

The Reynolds number dependency of secondary currents over rectangular ridges has received less attention since most studies have been conducted at fixed Reynolds number. By comparing the results of a direct numerical simulation at $Re_\tau = 500$ with experimental results at $Re_\tau = 4000$, Vanderwel et al. (2019) found that the induced secondary currents are similar for both cases. At both Reynolds numbers the same flow patterns were observed for the most energetic modes and the relative contributions of dispersive and turbulent stresses to the total shear stress were comparable. According to Vanderwel et al. (2019) the generation of secondary currents over ridge-type roughness is governed by outer scaling rather than inner (viscous) scaling, which is in line with results for strip-type roughness (Stroh et al. 2016). It should be noted that the compared configurations were at different spacings and performed only for a single value of ridge width and therefore the exact effect of Reynolds number on mean flow and turbulence statistics for fixed ridge configurations remains to be explored.

Ridge-type roughness comprised of ridges with other cross-sections have also been studied, although in less systematic manner. In general, it is presumed that SCs can be generated by any ridge shape, but the exact flow topology and strength of secondary currents are geometry

dependent (Wang and Cheng 2006). Medjnoun et al. (2020) investigated effects of ridge shape on secondary currents using ridges with triangular, semicircular, and rectangular cross-section at a fixed spacing. It was found that triangular ridges produce the strongest upwash above them, which extends further in the wall-normal direction compared to the other two shapes. Stroh et al. (2020a), who performed numerical study with triangular ridges that had concave sides, reported SCs of significantly higher magnitude and swirl strength compared to those generated by rectangular ridges in the studies by Vanderwel and Ganapathisubramani (2015) and Vanderwel et al. (2019). These results can be explained by the more favourable geometry of triangular ridges for deflecting flow upwards confirming that lateral ridge slope and flow deflection are important for formation of secondary currents (Goldstein and Tuan 1998; Wang and Cheng 2006).

For ridge shapes other than rectangular ridges, spanwise spacing is the main parameter that has been investigated to date (see, e.g., Zampiron et al. 2020), whereas the influence of other parameters, such as ridge width or Reynolds number, has mainly been studied for ridges with rectangular cross-section. Therefore, due to the limited number of systematic studies for other ridge shapes, it is unclear whether results obtained for rectangular ridges can be extrapolated to other ridge shapes. For example, comparing rectangular and triangular cross-sectional shapes, the former can be viewed as a section of the wall with a constant offset relative to the main wall, which allows for formation of secondary currents and tertiary flows above very wide ridges and in the valleys between them. In the latter case, the number of corners to which secondary currents are pinned is lower and the slope of ridge sides varies with ridge width. Therefore, the question regarding emergence of tertiary flows over side surfaces of triangular ridges with wide base remains open.

The present study aims to expand the knowledge on the behaviour of secondary currents generated by triangular ridge-type roughness by performing a numerical study using direct numerical simulations in a closed channel configuration. In the first part, the effects of ridge spacing on the topology and strength of secondary currents as well as mean flow and turbulence statistics are explored. To gain insight into the Reynolds number sensitivity of the secondary currents, the simulations are performed at two friction Reynolds numbers for each considered ridge spacing, an area where systematic studies are scarce. The results are compared to the data of Zampiron et al. (2020) who systematically studied the spacing effects for triangular ridges in an experimental study where ridges were placed on a rough bed in an open channel configuration. In the second part, the ridge base width is systematically varied to establish the influence of this parameter on the induced secondary currents, which to date has not been considered for ridges with triangular cross-section. To the best of the authors' knowledge, this is the first study on triangular ridges, where the effects of ridge base width as well as the Reynolds number sensitivity of ridge spacing on the emergence of large-scale secondary currents are systematically investigated using direct numerical simulations. The paper is structured as follows: the simulation approach, including the definition of the ridge geometry, studied configurations, and the DNS setup, is described in Sect.2. The main findings are presented and discussed in Sect.3. Conclusions are provided in Sect.4.

2 Methodology

Direct numerical simulations (DNS) of incompressible fully developed turbulent channel flow over systematically varied longitudinal ridges are performed to quantify the effects of spacing and ridge base width on the induced secondary currents. The DNS are performed

using the second order accurate finite difference DNS code iIMB (Busse et al. 2015). Streamwise, spanwise, and wall-normal velocity components are denoted by u , v , and w . The channel size is set to $3\pi\delta \times \pi\delta \times 2\delta$ in the streamwise (x), spanwise (y), and wall-normal (z) directions, where δ is the channel half-height (Fig. 1). The channel height, i.e., the distance between the lower and upper wall, is fixed to 2δ in all cases which is consistent with previous DNS studies of turbulent channel flow over streamwise ridges (see, e.g., Stroh et al. 2020a; von Deyn et al. 2021, 2022). The flow is driven by a constant mean pressure gradient, Π , based on which the mean friction velocity, u_τ , in the simulation is defined as $u_\tau = \sqrt{-\delta\Pi/\rho}$, where ρ is the constant density. The ridges are placed on both the lower and the upper channel walls and are mirrored with respect to the channel centre-plane. Periodic boundary conditions are imposed in the streamwise and spanwise directions, and the no-slip boundary condition is prescribed at the solid walls. The ridge-roughened surfaces are resolved using an iterative version of the embedded boundary method of Yang and Balaras (2006).

The first part of this study focusses on the influence of the ridge spacing, s , which is defined as the spanwise distance between tips of adjacent ridges (Fig. 1). The ridges have equilateral triangular cross-section with height $h/\delta = 0.08$. Four values of the ridge spacing, $s/\delta = \pi/8$, $s/\delta = \pi/4$, $s/\delta = \pi/2$, and $s/\delta = \pi$, are considered. To investigate the Reynolds number sensitivity of the results, DNS are conducted at two friction Reynolds numbers, $Re_\tau = u_\tau\delta/\nu$, where ν is the kinematic viscosity, namely 550 and 1000, for each ridge spacing. For both Re_τ , uniform computational grid spacing is applied in the streamwise and spanwise directions maintaining a spatial resolution of $\Delta x^+ < 5$ and $\Delta y^+ < 5$ in all simulations. The grid spacing in the spanwise direction is sufficiently fine to ensure a minimum of 16 grid points across the width of the ridge. This value is based on preliminary simulations conducted for the case with ridge spacing $s/\delta = \pi/2$ at $Re_\tau = 550$, where doubling number of grid points in the spanwise direction did not induce significant differences in terms of the mean flow and turbulence statistics. In the wall-normal direction, uniform grid spacing is applied up to the ridge crest ($\Delta z_{min}^+ = 2/3$), while above the grid spacing is gradually increased reaching its maximum value ($\Delta z_{max}^+ \approx 5$) at the channel centre. The details of the computational

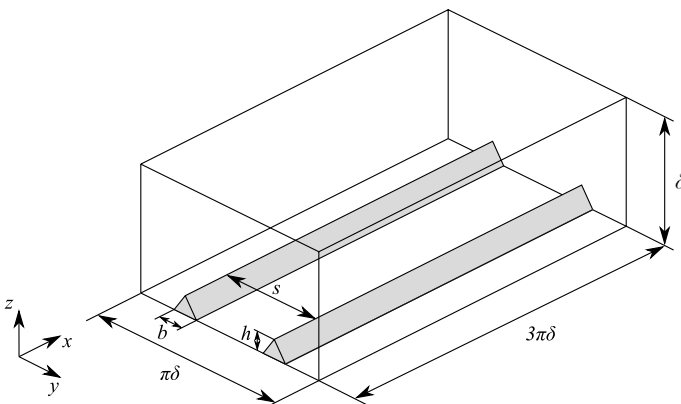


Fig. 1 Schematic (not to scale) of a channel with triangular ridges used for the DNS. δ is the channel half-height, h is the ridge height, b is the ridge base width, s is the spacing between adjacent ridges. The channel is symmetric with respect to the centre-plane and only the lower half of the channel is shown

grids, including number of grid points used for domain discretisation are summarised in Table 1. Reference smooth-wall simulations have been conducted at the same friction Reynolds numbers and their details are also included in Table 1. The dependency on the spanwise computational domain size was checked for the largest ridge spacing by conducting a simulation at $Re_\tau = 550$ using a computational domain where the spanwise width was doubled ($L_y = 2\pi$). The details of this simulation can be found in Table SI 1. The results (see Fig. SI 1) for the case with doubled domain size show very good agreement with the domain size used in the main study ($L_y = \pi$). In the following, for consistency all presented results are reported from simulations with $L_y = \pi$.

In the second part, the influence of the ridge base width, b , on secondary currents is investigated at a fixed ridge spacing $s/\delta = \pi/2$. This value of s/δ was chosen based on the results of the first part of this study, where at this spacing the SCs attained their maximum size. The ridge base width is systematically increased transforming the equilateral triangular cross-section with $b/\delta = 0.16/\sqrt{3}$ into an isosceles triangular cross-section. The ridge height remains constant in all simulations. First, the base width is increased to $b/\delta = \pi/4$, i.e., the ridges cover half of the channel wall, and then to $b/\delta = \pi/2$ covering the whole wall of the channel. In this part, the simulations are performed at a fixed friction Reynolds number of 550 and the same computational setup is adopted as for the spacing study at the same Re_τ (Table 1).

For each case, flow statistics are acquired for a minimum of 140 flow through times in all simulations at $Re_\tau = 550$ and for a minimum of 112 flow through times for simulations at $Re_\tau = 1000$ after the initial transient. Statistical quantities, such as Reynolds and dispersive stresses, are computed using a double-averaging approach (Raupach and Shaw 1982) which is applied in combination with intrinsic averaging (Gray and Lee 1977), i.e., only the fluid occupied region is considered when computing averages below the ridge crest. In the following $\bar{\cdot}$ indicates time-averaged quantities and $\langle \cdot \rangle$ indicates intrinsic spatial averaging over wall-parallel ($x - y$) planes.

Table 1 Parameters of the direct numerical simulations

Re_τ	L_x/δ	L_y/δ	L_z/δ	N_x	N_y	N_z	Δx^+	Δy^+	Δz_{min}^+	Δz_{max}^+
<i>Ridges</i>										
550	3π	π	2.00	1152	576	512	4.50	3.00	0.67	4.69
1000	3π	π	2.00	1920	640	896	4.91	4.91	0.67	5.02
<i>Smooth</i>										
550	8	4	2.00	896	448	512	4.91	4.91	0.50	3.87
1000	8	4	2.00	1536	768	896	5.21	5.21	0.50	4.08

L_x , L_y , and L_z are the domain sizes in streamwise, spanwise, and wall-normal direction; N_x , N_y , N_z are the number of grid points in the streamwise, spanwise, and wall-normal direction; Δx^+ and Δy^+ are the grid spacing in plus units in the streamwise and spanwise direction, Δz_{min}^+ and Δz_{max}^+ are the minimum and maximum grid spacing in plus units in the wall-normal direction

3 Results and Discussion

In this section the key results for the influence of ridge spacing, width, and friction Reynolds number are presented and discussed. First, the effects on the mean flow field and development of secondary currents are explored. Second, variation of the mean velocity profiles and turbulence statistics is examined. Finally, the changes in flow structure and streamwise velocity fluctuation are discussed using premultiplied streamwise energy spectra at different spanwise locations for surfaces with varied spacing.

3.1 Effects of Ridge Spacing and Reynolds Number on Mean Flow Fields and Secondary Currents

The influence of ridge spacing on the mean streamwise velocity field normalised by the centreline velocity (U_{cl}) is presented in Fig. 2. Values of the centreline velocity can be found in Table 2. For each case, results are shown at both friction Reynolds numbers,

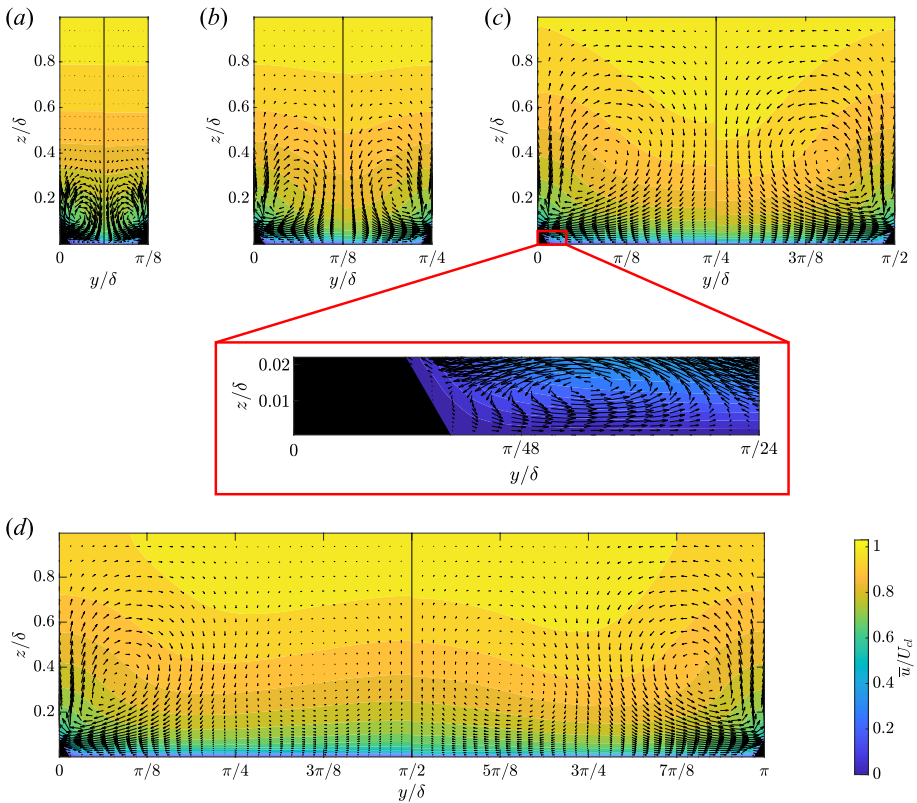


Fig. 2 Contours of the normalised phase-averaged mean streamwise velocity with superimposed in-plane velocity vectors, which are downsampled and scaled for clarity, for surfaces with varied ridge spacing: **a** $s/\delta = \pi/8$, **b** $s/\delta = \pi/4$, **c** $s/\delta = \pi/2$, **d** $s/\delta = \pi$. The left half of each panel shows results at $Re_\tau = 550$ and the right half at $Re_\tau = 1000$. Due to statistical symmetry with respect to the thin vertical black line only one half of the spanwise ridge pattern is shown for each Re_τ .

$Re_\tau = 550$ in the left half and $Re_\tau = 1000$ in the right half of the corresponding panels in Fig. 2. The changes in flow topology and strength of secondary currents with ridge spacing and Reynolds number are also identified and quantified through the magnitude of secondary currents, contours of which are shown in Fig. 3a–d, and time-averaged signed swirl strength presented in Fig. 3e–h. The magnitude of secondary currents is determined as $\sqrt{\bar{v}^2 + \bar{w}^2}/U_b$, where U_b is the bulk flow velocity (Stroh et al. 2020a, b). The signed swirl strength is computed as $\bar{\Lambda}_{ci} = \lambda_{ci}(\omega_x/|\omega_x|)$, where swirl strength λ_{ci} is defined as the imaginary part of the complex conjugate eigenvalue of the time-averaged velocity gradient tensor (Zhou et al. 1999) and inherits the sign of the time-averaged streamwise vorticity through multiplication by $(\omega_x/|\omega_x|)$. Therefore, $\bar{\Lambda}_{ci} > 0$ corresponds to clockwise rotation and $\bar{\Lambda}_{ci} < 0$ to counter-clockwise rotation.

As expected, triangular ridges generate SCs in the form of a pair of counter-rotating streamwise vortices. This vortex pair is symmetric with respect to the ridge and clearly evident from the in-plane velocity vectors (Fig. 2) and the vorticity-signed swirl strength (Fig. 3e–h). The upwash regions (LMPs) are located over the ridge crests, while the downwash flow (HMPs) is observed in the valleys in between ridges. The rotational direction of the secondary currents is preserved for all ridge spacings. The observed topology of secondary currents and their behaviour with ridge spacing are consistent with previous studies on the continuous streamwise ridges (see, e.g., Vanderwel and Ganapathisubramani 2015; Hwang and Lee 2018; Zampiron et al. 2020). For streamwise heterogeneous ridges, a swap in the location of upwash and downwash regions was reported by Yang and Anderson (2018) and Medjnoun et al. (2021) for $s/\delta \geq 1$. In the present study, no swap in the location of HMPs and LMPs is observed. This can be attributed to the different nature of the ridge geometry: the ridges investigated by Yang and Anderson (2018) and Medjnoun et al. (2021) were created by placing individual elements in series, namely truncated pyramids (Yang and Anderson 2018) or cuboids (Medjnoun et al. 2021). Thus, in addition to spanwise heterogeneity, these surfaces exhibited heterogeneity in the streamwise direction, which may induce the swap in the locations HMPs and LMPs at wide ridge spacing due to presence of a pressure drag component, which is absent in case of homogeneous ridges (Medjnoun et al. 2021).

At the lowest ridge spacing ($s/\delta = \pi/8$), secondary currents are readily observed (Fig. 2a). They are confined close to the ridge and are relatively small in size compared to the outer scale of the flow, i.e., δ , thus the flow field in the outer layer is not affected by SCs and remains homogeneous. This result is similar to the results of Zampiron et al. (2020) in open-channel flow and highlights the influence of ridge shape on formation of secondary currents. In particular, triangular ridges produce persistent SCs at smaller spacings compared to rectangular ridges, where SCs emerge for $s/\delta \gtrsim 0.5$ (Vanderwel and Ganapathisubramani 2015). With an increase in ridge spacing, first to $s/\delta = \pi/4$ and then to $s/\delta = \pi/2$, secondary currents progressively grow in size in both spanwise and wall-normal directions until they occupy the entire cross-section of the channel. This is accompanied by an increase in the level of spanwise heterogeneity of the mean flow with significant heterogeneity observed for the surface with $s/\delta = \pi/2$ (Fig. 2c). Spatial growth of SCs with ridge spacing is also reflected in the vorticity-signed swirl strength (Fig. 3e–g). Further increase in s/δ to π does not affect the size of the SC vortices, but results in the formation of an additional pair of counter-rotating streamwise vortices in the valley between ridges, commonly referred to as tertiary flows. These vortices are significantly weaker compared to the main secondary currents (Fig. 3h).

Stroh et al. (2020b) suggested that the strength of secondary currents can be estimated as the maxima of their magnitude, i.e., $\max(\sqrt{\bar{v}^2 + \bar{w}^2}/U_b)$. For $s/\delta = \pi$, the tertiary flows

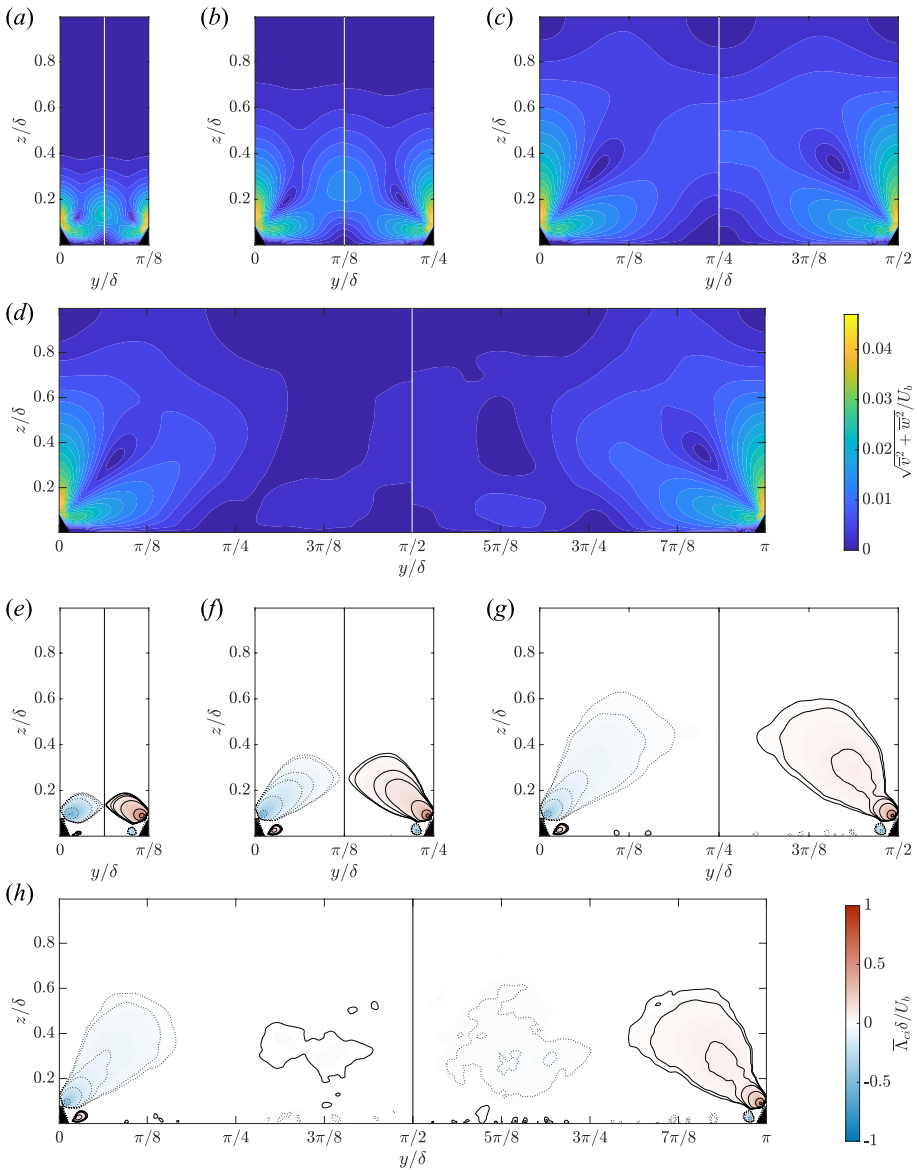


Fig. 3 Contours of the phase-averaged magnitude of the secondary currents (a–d) and mean signed swirl strength (e–h) for surfaces with varied ridge spacing: **a, e** $s/\delta = \pi/8$, **b, f** $s/\delta = \pi/4$, **c, g** $s/\delta = \pi/2$, **d, h** $s/\delta = \pi$. The left half of each panel shows results at $Re_\tau = 550$ and the right half at $Re_\tau = 1000$. Due to statistical symmetry with respect to the thin vertical white/black line only one half of the spanwise ridge pattern is shown for each Re_τ . Positive (solid) and negative (dotted) contour lines in e–h are shown at levels $\{0.01, 0.025, 0.07, 0.1, 0.2, 0.5, 0.75\}$ and $-\{0.01, 0.025, 0.07, 0.1, 0.2, 0.5, 0.75\}$

are approximately 12 times weaker at $Re_\tau = 550$ and 8 times weaker at $Re_\tau = 1000$). If instead comparing maximum swirl strength of secondary and tertiary vortices, following the approach by Vanderwel and Ganapathisubramani (2015), the secondary currents

are approximately 34 and 27 times stronger than the tertiary flows at $Re_\tau = 550$ and $Re_\tau = 1000$, respectively. For the present triangular ridges, the ratio of secondary to tertiary currents' strength is significantly higher compared to the factor of ≈ 2 reported by Vanderwel and Ganapathisubramani (2015) for rectangular ridges. This can be explained by a number of factors: first, as can be seen from the present results, tertiary flows become stronger with Reynolds number and at $Re_\tau = 4200$, which was used in Vanderwel and Ganapathisubramani (2015), the relative difference in secondary / tertiary currents' strength is expected to decrease. Second, due to their shape, triangular ridges produce more localised and stronger upwash flow compared to rectangular ridges. However, the downwash region is more spread across the valley and therefore is weaker, resulting in tertiary flows of lower strength. Third, comparing signed swirl strength contour maps from experiments by Vanderwel and Ganapathisubramani (2015) and those obtained in DNS by Hwang and Lee (2018) it can be noted that the region of the highest swirl strength around the ridge edges was outside the field of view in the experiments. This may have caused an underprediction of the maximum swirl strength for the secondary currents and thus the ratio of secondary to tertiary currents' strength.

For cases with narrow ridge spacing ($s/\delta \leq \pi/4$), an increase in Reynolds number from $Re_\tau = 550$ to $Re_\tau = 1000$ has only minor qualitative effects on flow topology and spanwise flow field heterogeneity (Figs. 2a and b and 3a and b). However, for surfaces with wide ridge spacing ($s/\delta \geq \pi/2$) and hence the most pronounced secondary currents, at $Re_\tau = 1000$ an increase over $Re_\tau = 550$ levels can be observed in the spanwise heterogeneity of the flow due to elevated mean flow speed in HMPs regions (see also Fig. 3a–d). The signed swirl strength of SCs also increases with Reynolds number (Fig. 3e–h), but this increase is observed mainly in the core region of the SCs, while at the outer edges it remains largely insensitive to Re_τ . The tertiary flows show a stronger Reynolds number sensitivity and intensify with increase in Re_τ .

Irrespective of the ridge spacing and Re_τ , the highest magnitude of secondary currents is found in the upflow regions over the ridges (Fig. 3a–d). At the lowest tested spacing, the strength of SCs is approximately 4.1% of the bulk flow velocity at $Re_\tau = 550$. As the spacing is increased to $\pi/4$, SCs strength reaches approximately 4.4% of U_b and remains almost unaffected as the ridges are placed further apart. At $Re_\tau = 1000$, the same trend with variation of ridge spacing holds, but SCs become stronger reaching 4.3% of U_b at $s/\delta = \pi/8$ and 4.6% at the higher values of s/δ . The present results are consistent with 4.4% reported in the experimental study of Medjnoun et al. (2020) for triangular ridges of the same height in outer units ($h/\delta = 0.08$) at spacing of $s/\delta = 1$. In the context of other ridge shapes, the present values are higher compared to 2.2% – 3.3% found for semicircular and rectangular ridges of various widths with similar heights ($h/\delta = 0.08 - 0.09$) in the experimental study by Medjnoun et al. (2020). This is consistent with the observation of Wang and Cheng (2006) that a triangular ridge shape enhances upward deflection of the flow and thus the strength of secondary currents. SCs of even higher strength (6.6%) have been reported for triangular ridges with concave sides (Stroh et al. 2020a). However, it should be noted that Stroh et al. (2020a) used twice taller ridges with $h/\delta = 0.16$, which in addition to the concave sides may have increased the strength of SCs.

The changes in flow topology with spacing and Reynolds number are quantified by measuring the wall-normal elevation of the centres of the SCs above the ridge tips ($(z_{sc} - h)/\delta$). The centres of secondary currents move towards the channel centre-plane as the spacing is increased from $\pi/8$ to $\pi/2$ and the SCs grow in size (Fig. 4a). At both Re_τ , the change in $(z_{sc} - h)/\delta$ follows a linear trend over this range of spacing, which is consistent with the experimental results of Zampiron et al. (2020) for triangular ridges with

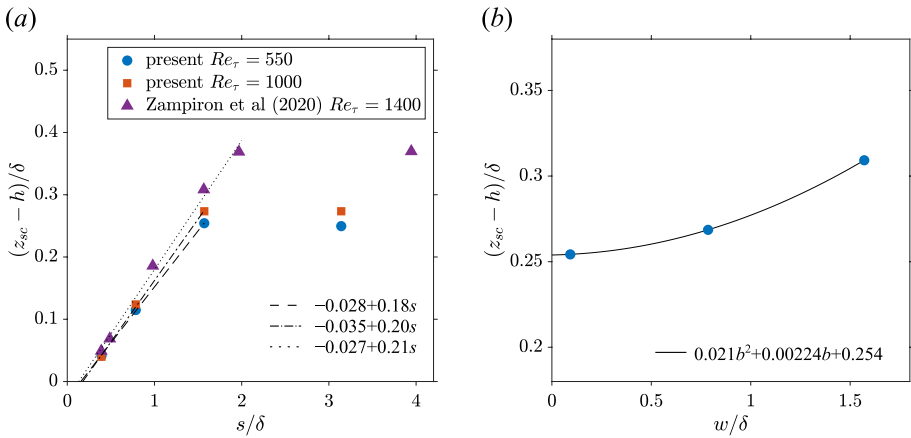


Fig. 4 Wall-normal elevation of secondary current centres as a function of **a** ridge spacing at different Re_τ and **b** ridge width at $Re_\tau = 550$. Experimental results from Zampiron et al. (2020) for triangular ridges in open channels with rough beds are included in part (a)

$h/\delta = 0.12$ at $Re_\tau = 1400$. At the lowest ridge spacing, the wall-normal elevation of SCs matches between the experiments and the present DNS data and does not exhibit sensitivity to Re_τ . However, for cases with pronounced SCs, Reynolds number appears to influence the dependency of $(z_{sc} - h)/\delta$ on the spacing s/δ . With higher Re_τ , the slope in the linear relationship between $(z_{sc} - h)/\delta$ and s/δ increases (see Fig. 4a). At the maximum tested ridge spacing ($s/\delta = \pi$), where tertiary flows are present, no significant change in $(z_{sc} - h)/\delta$ is observed compared to $s/\delta = \pi/2$. This is consistent with the data of Zampiron et al. (2020) and confirms that the secondary currents have already reached their maximum size. However, the maximum value of $(z_{sc} - h)/\delta$ is consistently lower in the present DNS compared to the experimental result of Zampiron et al. (2020). This can be attributed to the different flow configurations, namely closed channel in the DNS versus open channel in the experiments. In contrast to an open channel flow with a free water surface, in a closed symmetric channel configuration, the wall-normal growth of secondary currents is restricted by SCs generated on the opposite wall. Dependency of secondary current elevation on the specific channel configuration can also be found in the study of Stroth et al. (2020a) where secondary currents in a closed symmetric channel displayed lower elevation compared to a closed channel case with identical ridge configuration where the pattern was shifted by $s/2$ on the upper wall breaking the symmetry with respect to the centre-plane.

In addition to the dominant secondary current vortices, the presence of small vortices formed in the corner between the lateral ridge surface and the channel wall can be observed on each side of the ridge. In Fig. 2 only one of these vortices is shown as the inset to part (c), but these corner vortices can be clearly observed for each considered ridge spacing and Re_τ in the mean signed swirl strength fields in Fig. 3e–h. Castro et al. (2021) recently reported similar corner vortices for rectangular ridges and pointed out that sufficient grid resolution is required to resolve these features. It is therefore not unexpected that similar vortices are also observed for the present configurations, but - to the best of our knowledge - corner vortices have not previously been reported for triangular ridge geometries. The corner vortices are weaker compared to the secondary currents but stronger than the tertiary flows; the size and strength of the corner vortices appear to be consistent across most

of the considered values of s/δ and Re_τ . Similar corner vortices may well be present for other ridge shapes, but they would be difficult to observe in experiments due to their very close proximity to the wall and their small size.

3.2 Effects of Ridge Width on Mean Flow Fields and Secondary Currents

The effects of ridge width on the mean streamwise velocity field normalised by U_{cl} and the signed swirl strength are shown in Fig. 5. As the ridges become wider, the base region of secondary currents remains attached to lateral surfaces of the ridge, expanding with b/δ , while the wall-normal extent of SCs is not affected. Overall, the SCs assume a more square shape as ridge width is increased. The swirl strength of secondary currents decreases as b/δ is increased. Similar trends have been reported for rectangular ridges (Hwang and Lee 2018; Medjnoun et al. 2020). However, in contrast to rectangular ridges, no tertiary flows are found to form over wide triangular ridges even for the widest tested ridge with $b/\delta = \pi/2$. This key difference in flow topology between triangular and rectangular ridges can be explained by the difference in cross-sectional geometry: with respect to the cross-stream plane for a triangular ridge there is only a single corner to which SCs are pinned, whereas two exposed, SCs-generating, corners separated by an elevated smooth-wall section are present for a rectangular ridge. Increase in ridge width also affects the wall-normal elevation of the centres of SCs. Similarly to spacing, increase in b/δ moves SCs centres higher above the ridges (Fig. 4b). However, in this case the variation of $(z_{sc} - h)/\delta$ appears to follow a quadratic polynomial rather than a linear trend.

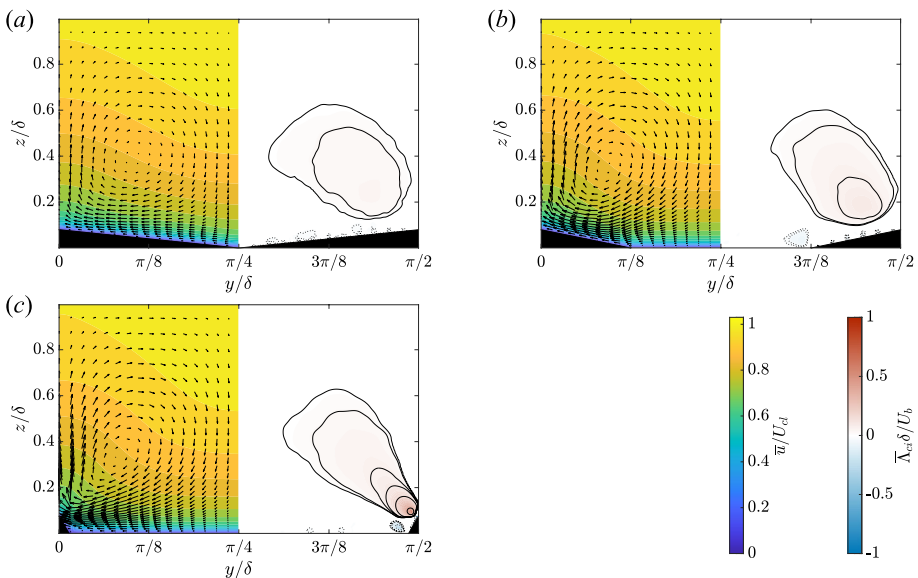


Fig. 5 Mean flow fields for varied ridge base width. Left half of each panel: contours of normalised phase-averaged mean streamwise velocity with superimposed in-plane velocity vectors (downsampled and scaled for clarity); right half of each panel: mean signed swirl strength. **a** $b/\delta = \pi/2$, **b** $b/\delta = \pi/4$, and **c** $b/\delta = 0.16/\sqrt{3}$ (the latter repeated from Figs. 2c and 3g). Statistical symmetry with respect to $y/\delta = \pi/4$ applies in all cases. Positive (solid) and negative (dotted) contour lines for swirl strength are shown on the levels $\{0.01, 0.025, 0.07, 0.1, 0.2, 0.5, 0.75\}$ and $-\{0.01, 0.025, 0.07, 0.1, 0.2, 0.5, 0.75\}$

The corner vortices forming at the intersection between the lateral sides of the ridges and the smooth-wall sections are also affected by the ridge width. As b/δ is increased to $\pi/4$ they expand in size and their strength reduces (Fig. 5b). For the widest ridge ($b/\delta = \pi/2$) they disappear. In this case, no smooth-wall sections remain in between ridges, and thus the number of corners in between ridge crests is reduced by one. Effectively, as the ridge width increases, the corner vortices move further towards the centre location in between ridge crests weakening in strength until they ultimately cancel each other and disappear when the ridge width matches the ridge spacing.

3.3 Effects of Ridge Spacing and Reynolds Number on Mean Flow and Turbulence Statistics

The streamwise velocity profiles for all ridge spacings are shown in Fig. 6a. As s/δ is increased, the downward shift in the velocity profile with respect to the smooth-wall data is reduced. With increase in Re_τ , surfaces with wide ridge spacing show a stronger Reynolds number sensitivity of ΔU^+ compared to those with narrow ridge spacing. At the lowest spacing ($s/\delta = \pi/8$), no change in ΔU^+ is recorded (Table 2). The value of ΔU^+ is estimated as the downwards shift in the mean streamwise velocity profile measured at the channel centre-plane. Alternatively, ΔU^+ can be estimated from the skin friction coefficient (C_f) as $\Delta U^+ = (\sqrt{2/C_f})_s - (\sqrt{2/C_f})_r$ (Granville 1987), where the subscript s denotes ‘smooth’ wall, r ‘rough’ wall, and $C_f = 2(u_\tau/U_b)^2$. Although this measure will result in slightly different values of ΔU^+ , the overall trends with variation in ridge spacing are

Table 2 Mean flow quantities for all cases

s/δ	b/δ	Re_τ	U_{cl}	U_b	Re	ΔU^+	$C_f \times 10^{-3}$
<i>Varied ridge spacing</i>							
$\pi/8$	$0.16/\sqrt{3}$	550	19.58	16.60	18,260	1.59	7.26
$\pi/8$	$0.16/\sqrt{3}$	1000	21.18	18.09	36,180	1.59	6.11
$\pi/4$	$0.16/\sqrt{3}$	550	19.95	17.32	19,052	1.22	6.67
$\pi/4$	$0.16/\sqrt{3}$	1000	21.27	18.66	37,320	1.49	5.74
$\pi/2$	$0.16/\sqrt{3}$	550	20.09	17.75	19,525	1.08	6.35
$\pi/2$	$0.16/\sqrt{3}$	1000	21.30	19.09	38,180	1.47	5.49
π	$0.16/\sqrt{3}$	550	20.68	18.17	19,987	0.49	6.06
π	$0.16/\sqrt{3}$	1000	21.93	19.56	39,120	0.83	5.23
<i>Varied ridge base width</i>							
$\pi/2$	$\pi/4$	550	20.20	17.56	19,316	0.97	6.49
$\pi/2$	$\pi/2$	550	20.20	17.09	18,799	0.96	6.85
<i>Smooth wall</i>							
–	–	550	21.17	18.54	20,394	–	5.82
–	–	1000	22.76	20.11	40,220	–	4.95

U_{cl} , centreline velocity; U_b , bulk flow velocity; $Re = 2\delta U_b/\nu$, bulk flow Reynolds number; ΔU^+ , downward shift in the mean velocity profile measured at the channel centre-plane; C_f , skin friction coefficient

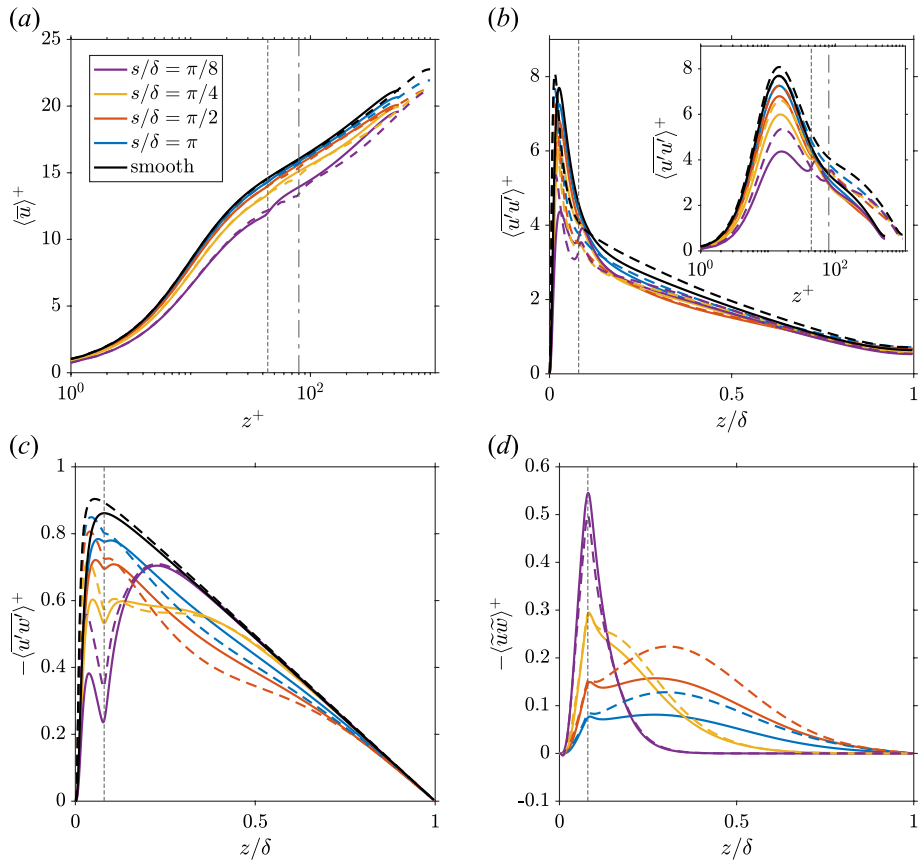


Fig. 6 Profiles of streamwise velocity (a), streamwise Reynolds normal stress (b), and Reynolds (c) and dispersive (d) shear stress profiles for surfaces with varied ridge spacing at $Re_\tau = 550$ (solid lines) and $Re_\tau = 1000$ (dashed lines). Reference smooth-wall data is shown with black lines. Location of the ridge crest is marked by thin dashed ($Re_\tau = 550$) and dash-dotted ($Re_\tau = 1000$) vertical lines. The legend in part a applies to all parts of the figure

preserved. It should be noted, that large ridge spacings and consequently the presence of space-filling secondary currents modify the mean velocity profiles over the surfaces and thus result in a loss of outer-layer similarity (see below). As pointed out by Endrikat et al. (2022) for this type of surface, the interpretation of ΔU^+ as roughness function therefore becomes questionable. A deviation from the smooth-wall log-law is observed for most cases, and this deviation increases as the spacing is reduced. The values of ΔU^+ and C_f suggest that all surfaces are in the transitionally rough regime. However, as was discussed by Vanderwel et al. (2019), there may be no fully-rough regime for uniform streamwise ridge-type roughness due to lack of the pressure drag component, which constitutes the dominant drag contribution in the fully rough regime for conventional roughness.

The streamwise velocity profiles in defect form are shown in Fig. 7 for both Reynolds numbers. When taking the virtual wall origin at the channel wall ($z_0 = 0$), only the surface with $s/\delta = \pi/4$ yields a good collapse with the smooth-wall data at both Re_τ . For the other surfaces absence of collapse is observed up to $z/\delta \gtrsim 0.6$. Considering the

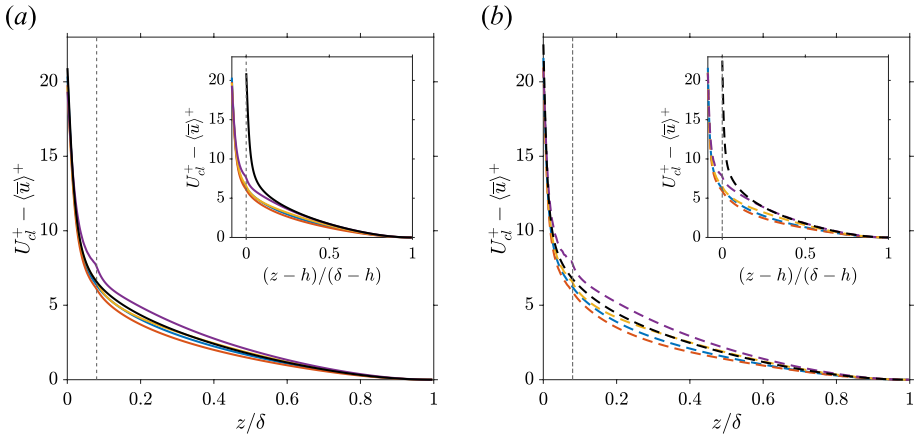


Fig. 7 Streamwise velocity defect profiles for surfaces with varied ridge spacing at $Re_\tau = 550$ **a** and $Re_\tau = 1000$ **b** with virtual wall origin taken at the channel wall ($z_0 = 0$). The insets in each panel show the same profiles but with virtual wall origin taken at the ridge crests ($z_0 = h$). Line styles are the same as in Fig. 6

usual range of wall origins for rough surfaces, which falls between the channel wall and roughness height, we have tested the other end of this range, by setting the virtual wall origin to the ridge crest ($z_0 = h$). This leads to significant improvement in the levels of outer layer similarity for the case with the narrowest ridge spacing $s/\delta = \pi/8$ at both Reynolds numbers (see insets in Fig. 7). However, for the other cases, including the surface with ridge spacing $s/\delta = \pi/4$, the collapse with the smooth-wall profile worsens. It appears that the initial growth of secondary currents (before they become space-filling) due to increase in ridge spacing shifts the virtual wall origin from the top of the ridge crests (case $s/\delta = \pi/8$) to the bottom wall of the channel (case $s/\delta = \pi/4$). For these two cases, some degree of outer layer similarity can be recovered, since above the secondary currents there is still a region of the flow unaffected by the dispersive stresses associated with them. For the cases with ridge spacing $s/\delta \geq \pi/2$, where the secondary currents extend to the channel centre-plane, outer layer similarity is not expected. These results for the outer behaviour of the velocity profile are in line with previous findings for ridge-type roughness, which showed that the presence of space-filling secondary currents breaks outer layer similarity due to elevated levels of dispersive stresses which propagate into the outer flow (Chan et al. 2018; Medjnoun et al. 2020, 2021).

The streamwise Reynolds normal stress ($\overline{u'u'}$) profiles are presented in Fig. 6b. Below the ridge crests, a peak in $\overline{u'u'}$ is observed at the same location where the $\overline{u'u'}$ profile peaks in the smooth-wall case. It can thus be associated with the smooth sections of the channel in between ridges. The levels of $\overline{u'u'}$ below the ridge crests increase with s/δ and approach the smooth-wall case for the highest spacing. This is consistent with the increase in the size of the flat wall sections as ridge spacing increases. As in the smooth-wall case, an increase in the peak streamwise normal Reynolds stress can be observed with Re_τ , with a slightly stronger Reynolds number sensitivity becoming apparent as ridge spacing is reduced. For surfaces with $s/\delta \leq \pi/4$ a second peak just above ridge crest can be observed at both Re_τ . Above the ridge crest, $\overline{u'u'}$ decreases as ridges are placed further apart, however, a slight recovery in $\overline{u'u'}$ levels can be observed as tertiary flows emerge. In the outer region, a reduction in $\overline{u'u'}$ compared to

smooth-wall levels can be seen for all cases. Streamwise Reynolds normal stresses will be discussed further in Sect. 3.5.

Of all Reynolds and dispersive stress profiles, the ridge spacing has the most pronounced effect on the Reynolds $\langle \overline{u'w'} \rangle$ and dispersive $\langle \widetilde{u\widetilde{w}} \rangle$ shear stress profiles, which are shown in Fig. 6c and d. At the lowest ridge spacing ($s/\delta = \pi/8$), dispersive momentum fluxes emerge above the ridge crest indicating the presence of SCs. As s/δ is increased they extend further away from the ridge crests and almost reach up to the channel centre-plane for $s/\delta \geq \pi/2$, thus reflecting the spatial development of SCs. With an increase in ridge spacing from $\pi/8$ to $\pi/2$, the levels of Reynolds shear stress in the outer layer drop (Fig. 6c) and this drop is compensated by an increase in the dispersive shear stress (Fig. 6d). However, at the maximum tested ridge spacing ($s/\delta = \pi$), where tertiary flows are present, some recovery in the $\langle \overline{u'w'} \rangle$ profile is observed, where levels of dispersive shear stress are reduced compared to the case with $s/\delta = \pi/2$. Overall, the dependency of $\langle \overline{u'w'} \rangle$ and $\langle \widetilde{u\widetilde{w}} \rangle$ above the ridge crest on ridge spacing is similar at both friction Reynolds numbers and is consistent with the experimental findings of Zampiron et al. (2020) for triangular ridges.

The present DNS also provide insight into the behaviour of the shear stresses just above and below the ridge crest, a region of the flow which is difficult to access in experiments. Figure 6c shows that $\langle \overline{u'w'} \rangle$ progressively increases with ridge spacing in this region. At all considered values of s/δ , the Reynolds shear stress profiles exhibit a double-peak behaviour, with the first peak located below the ridge crest and the second above (Fig. 6c). At the narrowest ridge spacing, a clear separation between these two peaks is observed, and the magnitude of the peak located below the ridge crest is significantly smaller than for the peak above. As the spacing is increased, the separation between peaks reduces, while the magnitude of the first peak increases and exceeds the above crest peak for $s/\delta \geq \pi/4$. The observed behaviour can be explained by considering the changes in the spatial distribution of the Reynolds shear stress with s/δ presented in Fig. 8a–d. As ridge spacing grows, larger smooth-wall sections between the ridges are exposed to the flow, and the $u'w'$ levels over this part of the channel progressively increase. For all cases, the maximum value of the local Reynolds shear stress is observed directly above the ridge crest with elevated values extending almost up to the channel centre-plane. This distribution of $\overline{u'w'}$ appears to be universal for ridge-type roughness (Vanderwel and Ganapathisubramani 2015; Hwang and Lee 2018; Zampiron et al. 2020). The spatial distribution of the dispersive shear stress is shown in Fig. 8e–h. As for the Reynolds shear stress, elevated levels of $\widetilde{u\widetilde{w}}$ are correlated with the upflow regions over the ridge crests. In addition, areas of elevated dispersive shear stresses, although of lower magnitude, are observed in the downflow regions. Increase in Re_τ results in higher magnitude of $\widetilde{u\widetilde{w}}$ above ridge crests, which, as discussed below, is also reflected in the corresponding profiles. In addition, the size of both regions affected by the elevated levels of dispersive shear stress increases with Re_τ , especially in the cases with the largest SCs. While in the upwash regions affected areas grow in size mainly in the wall-normal direction, in the downwash-associated regions they expand in both wall-normal and spanwise direction (see Fig. 8g and h).

Change in Re_τ has considerable effect on the Reynolds and dispersive shear stresses, especially for the cases with the most pronounced secondary currents. For the surface with the narrowest ridge spacing, increase in Re_τ leads to elevation of $\langle \overline{u'w'} \rangle$ only below and immediately above the ridge crest, whereas the $\langle \widetilde{u\widetilde{w}} \rangle$ profile follows an opposite trend. As the ridges are placed further apart and secondary currents grow in size, the increase in dispersive shear stress levels above the ridge crest becomes more significant and propagates further away from the ridge (Fig. 6d). The magnitude of increase in $\langle \widetilde{u\widetilde{w}} \rangle$ with Re_τ

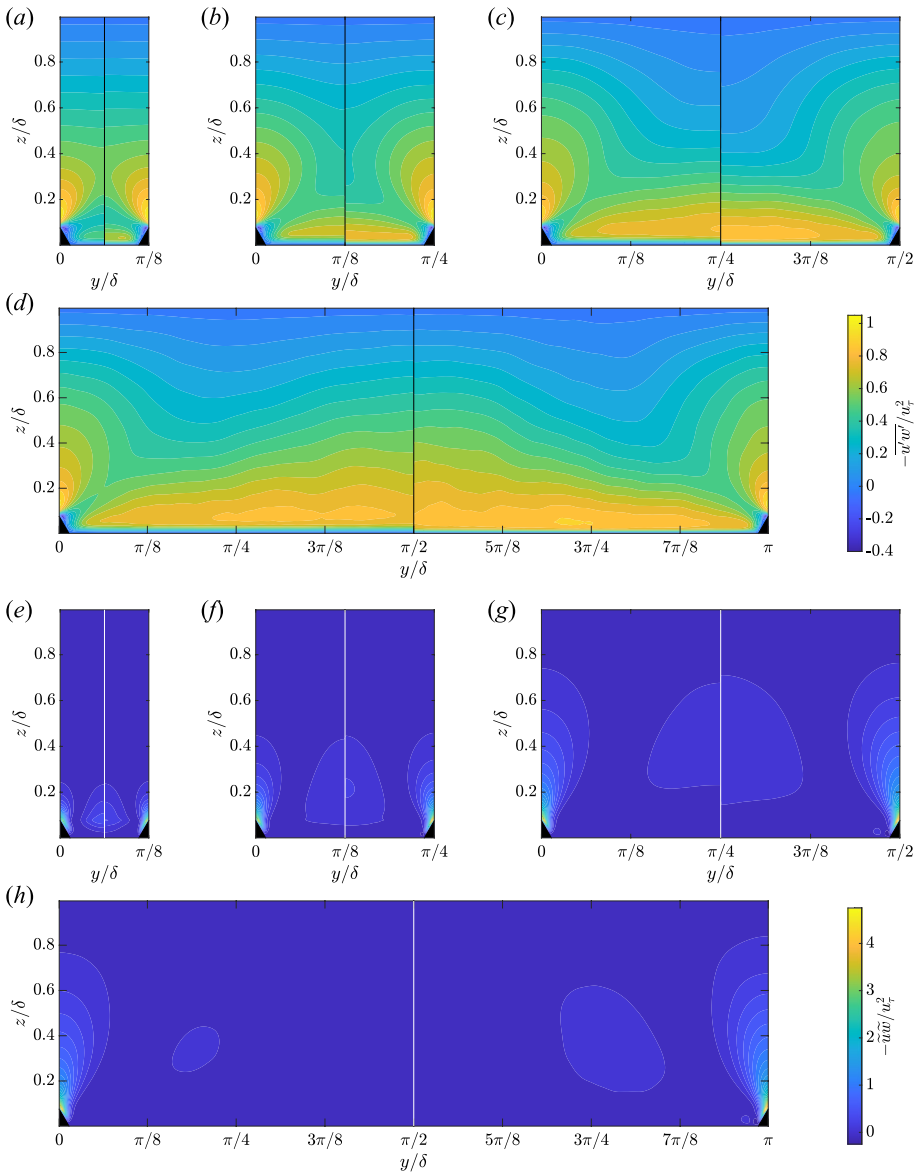


Fig. 8 Contours of phase-averaged mean Reynolds (a–d) and dispersive (e–h) shear stresses for surfaces with varied ridge spacing: a, e $s/\delta = \pi/8$, b, f $s/\delta = \pi/4$, c, g $s/\delta = \pi/2$, d, h $s/\delta = \pi$. The left half of each panel shows results at $Re_\tau = 550$ and the right half at $Re_\tau = 1000$. Due to statistical symmetry with respect to the thin vertical white/black line only one half of the spanwise ridge pattern is shown for each Re_τ

depends on s/δ with the highest change observed for $s/\delta = \pi/2$, where SCs have reached their maximum size. In contrast, the $\langle \widetilde{uw} \rangle$ levels below the ridge crests are not affected by Re_τ for $s/\delta \geq \pi/4$. Exactly opposite trends are observed for the $\langle u'w' \rangle$ profiles above the ridge crest as spacing is varied from $s/\delta = \pi/4$ to $s/\delta = \pi$, while below and just above the crest, Reynolds shear stress levels increase with Re_τ . Comparing the present shear stress

profiles to the experimental data of Zampiron et al. (2020) at higher Reynolds number ($Re_\tau = 1400$), Reynolds number dependency over the broader range can be extrapolated. For example, at matched value of $s/\delta = \pi/2$, the maximum value of the dispersive shear stress at $Re_\tau = 1000$ is 0.22, while at $Re_\tau = 1400$ it reaches ≈ 0.3 . However, it cannot be excluded that difference between the open and closed channel configuration, which was found to affect the location of SCs centres (see above), could also influence the shear stress statistics.

These findings contrast with the observations of Vanderwel et al. (2019), who reported no significant Reynolds number sensitivity of secondary currents and shear stresses for rectangular ridges. There could be a number of reasons for the differing conclusions regarding Reynolds number sensitivity. First, a different ridge shape is considered in the present study and the stronger SCs induced by triangular ridges could intensify further with Re_τ , while those produced by rectangular ridges may reach their limit at lower Re_τ . Second, Vanderwel et al. (2019) compared results for two surfaces with different ridge spacings, namely with $s/\delta = 0.88$ from experiments at $Re_\tau = 4000$ and $s/\delta = 1$ from the DNS at $Re_\tau = 500$. This mismatch in ridge spacing limits a direct comparison of turbulence statistics and thus conclusions regarding Reynolds number sensitivity. Finally, the difference in the flow configuration could also affect the comparison, i.e., the experimental data were obtained for a turbulent boundary layer, while the DNS was performed in a half-channel with symmetry boundary condition applied at the channel centre-plane. Further studies will be required to elucidate the interrelationship between the influence of Reynolds number, ridge shape, spacing, and flow configuration on SCs.

3.4 Reynolds and Dispersive Shear Stresses for Surfaces with Varied Ridge Width

Similarly to ridge spacing, variation of the ridge width has strong effects on the Reynolds and dispersive shear stress profiles (see Fig. 9). As the ridges widen, the levels of $\langle u'w' \rangle$ below and immediately above the ridge crest progressively drop, and the near-wall peak, associated with the flat sections between the ridges, decreases in magnitude (Fig. 9a). This is the result of a reduction of the flat wall area between the ridges. For

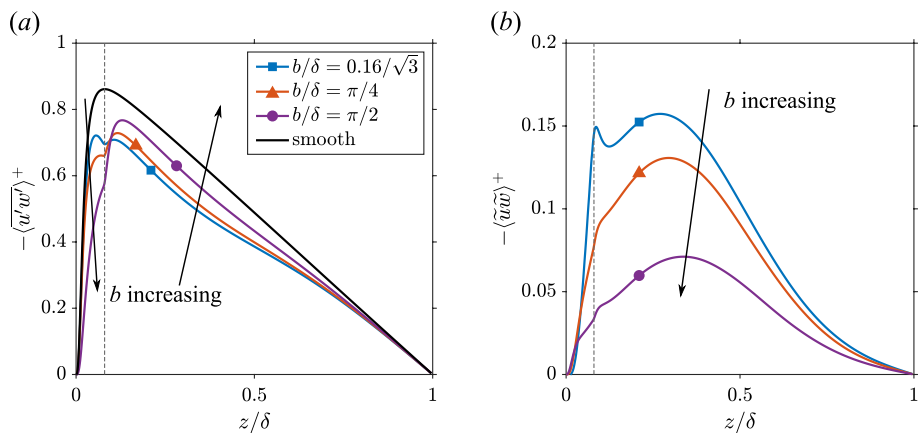


Fig. 9 Reynolds (a) and dispersive (b) shear stress profiles for surfaces with varied ridge base width at $Re_\tau = 550$. Reference smooth-wall data is shown with a black line. The location of the ridge crest is marked by a thin dashed vertical line. The legend in part a applies to both parts of the figure

the widest ridge case with $b/\delta = \pi/2$, where ridges cover the entire wall, no distinct near-wall peak can be observed in the $\langle u'w' \rangle$ profile. Dispersive shear stresses are also reduced below the ridge crest as b/δ increases except in the immediate vicinity of the wall, i.e., for $z/\delta \approx 0$, where an opposite trend is observed (Fig. 9b). Above the ridge crest, Reynolds shear stress levels increase with widening of the ridge. However, none of the cases collapse onto the smooth-wall profile with deviations observed almost up to the channel centre-plane.

The changes in the $\langle u'w' \rangle$ profiles above the ridge crest are matched by corresponding changes in the $\langle \tilde{u}\tilde{w} \rangle$ profiles. The highest $\langle \tilde{u}\tilde{w} \rangle$ levels above the ridge crest are observed for the narrowest ridge case, where the maximum value of the dispersive shear stress exceeds the widest ridge case by almost a factor of three (Fig. 9b). This drop mainly occurs due to a decrease in dispersive shear stress levels in the upflow regions above the ridges with increasing ridge width, as can be observed from the spatial distribution of $\tilde{u}\tilde{w}$ (see Fig. 10). The region of elevated dispersive shear stress in the centre of the valley between ridges is unaffected as b/δ is increased to $\pi/4$. For the largest ridge width ($b/\delta = \pi/2$), where the flat section between ridges is eliminated, this region narrows in the spanwise direction and approaches the ridge surface. This can be associated with the observed small increase in dispersive shear stress profiles in the immediate vicinity of the wall that was mentioned in the discussion above. For the largest ridge width, the magnitude of $\tilde{u}\tilde{w}$ is similar in both regions of elevated values, since $\tilde{u}\tilde{w}$ levels in the region above the ridge decrease with the ridge width. This trend is consistent with similar observations for rectangular ridges of increasing width by Medjnoun et al. (2020).

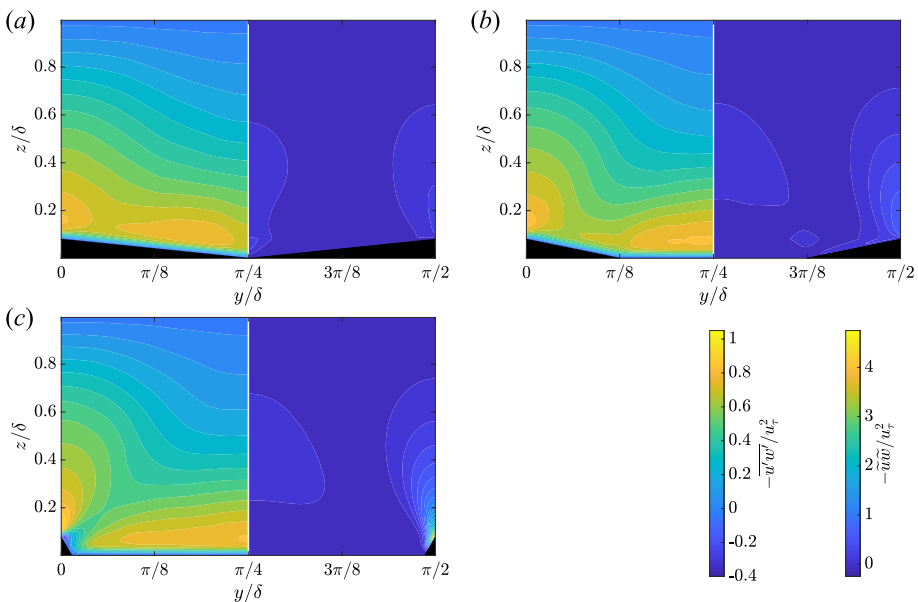


Fig. 10 Contours of the phase-averaged mean Reynolds (left half of each panel) and dispersive (right half of each panel) shear stresses for surfaces with varied ridge base width: **a** $b/\delta = \pi/2$, **b** $b/\delta = \pi/4$, **c** $b/\delta = 0.16/\sqrt{3}$ (the latter repeated from Fig. 8c and g). Statistical symmetry of the fields with respect to $y/\delta = \pi/4$ applies in all cases

3.5 Effects of Ridge Spacing on Premultiplied Velocity Spectra

The changes in the streamwise velocity fluctuations and flow structure with ridge spacing are explored further using premultiplied streamwise energy spectra $k_x \phi_{uu} / u_\tau^2$ (see Fig. 11). Following Zampiron et al. (2020), $k_x \phi_{uu} / u_\tau^2$ is shown for three selected spanwise locations, which correspond to the ridge centreline (left column in Fig. 11), the location of secondary current centres (middle column in Fig. 11), and the centre of the valley between ridges (right column in Fig. 11). This representation is chosen since contribution of SCs are difficult to discern from contours of premultiplied streamwise energy spectra when presented in their usual, spanwise-averaged, form (see Fig. SI 2). The spectra were computed using

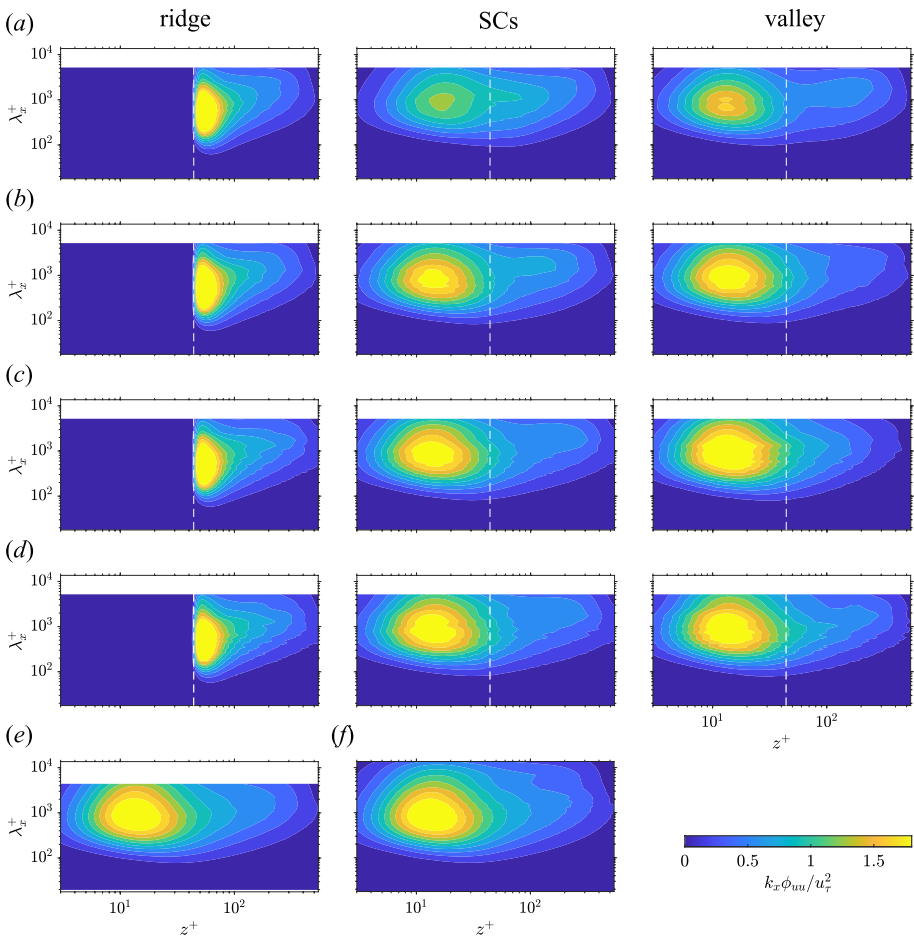


Fig. 11 Premultiplied streamwise energy spectra $k_x \phi_{uu} / u_\tau^2$ at $Re_\tau = 550$ as a function of streamwise wavelength (λ_x) and wall-normal location (z) for surfaces with varied ridge spacing **a** $s/\delta = \pi/8$, **b** $s/\delta = \pi/4$, **c** $s/\delta = \pi/2$, **d** $s/\delta = \pi$ at three different spanwise locations: ridge centreline (left column), location of secondary current centres (middle column), and centre of the valley between ridges (right column). The thin white dashed line marks the wall-normal location of the ridge crest. Reference smooth-wall data is shown in (e). In addition, data from the channel flow DNS of Lee and Moser (2015) at $Re_\tau = 550$ for a larger domain size is included in (f)

2000 instantaneous snapshots separated by 22 viscous time units ($\Delta t^+ = \Delta t u_\tau^2 / \nu$) that were acquired in each simulation at $Re_\tau = 550$. Reference smooth-wall data are shown in Fig. 11e for the present smooth-wall case; the spectrum from the DNS by Lee and Moser (2015) at $Re_\tau = 550$ for a larger domain size is also shown (see Fig. 11f).

At the ridge centreline location, which also corresponds to the upwash region of the flow, an energy peak just above the ridge crest is observed in all cases. This peak reflects elevated levels of $u'u'$ close to the ridge surface due to high local drag and is consistent with previous studies on rectangular ridges where high levels of streamwise velocity fluctuations in this region were observed (Vanderwel and Ganapathisubramani 2015; Hwang and Lee 2018). Elevated energy levels propagate further away from the ridges as spacing is increased up to $s/\delta = \pi/2$ and SCs grow and consequently produce more pronounced upwash motions at this location.

At the other two considered spanwise locations, i.e., at the location of the secondary current centres and in the centre of the valley between ridges, a clear peak below the ridge crest is observed. The location of this peak ($\lambda_x^+ \approx 1000$ and $z^+ \approx 15$) corresponds to the smooth-wall inner peak, which is associated with the near-wall cycle (Jiménez and Pinelli 1999; Monty et al. 2009). The magnitude of this peak decreases as ridges are placed closer together indicating that the near-wall cycle becomes less energetic. When comparing spectra at these spanwise locations at heights above the ridge crests, an increase in the energy contributions at large streamwise wavelengths is observed for all s/δ at the location of SCs. The wall-normal extent of the region with increased energy matches the size of secondary currents in this direction at the corresponding spacing, indicating that it is caused by the presence of SCs in the flow. A similar increase in the energy at high wavelength due to secondary currents was reported by Chan et al. (2018) for DNS of turbulent pipe flow. Elevated levels observed at the valley location for $s/\delta = \pi/8$ (Fig. 11a) are a result of a close proximity of SCs generated on the sides of two adjacent ridges (see Fig. 3e) and can also be observed in the experimental results of Zampiron et al. (2020) at low ridge spacing.

The present results emphasise that the spanwise flow heterogeneity observed in the mean flow fields is also reflected in the spectra of the instantaneous velocity fluctuations. Highly localised upflow regions above the ridge crests enhance the turbulent kinetic energy while the spreaded downflow regions in the valleys show reduced levels of turbulent kinetic energy but contain elevated energy contributions at high wavelengths. To see a clearer picture of the contribution of secondary currents a much longer domain in the streamwise direction would be required, which is currently not feasible for systematic studies using DNS. Increase in Re_τ does not significantly change the structure of secondary flows and the observed trends and dependency of spectra on the spanwise location are very similar to the results discussed for $Re_\tau = 550$. The premultiplied spectra for all cases at $Re_\tau = 1000$ can be found in Figs. SI 3 and 4.

4 Conclusions

The influence of ridge spacing and base width on secondary currents, mean flow, and turbulence statistics have been systematically studied using direct numerical simulations of turbulent channel flow over streamwise aligned ridges with triangular cross-section. Overall, the development and topological changes in SCs with ridge spacing are consistent with previous results for ridge-type roughness composed of streamwise homogeneous ridges, including the emergence of tertiary flows for very wide spacing (Vanderwel and

Ganapathisubramani 2015; Hwang and Lee 2018; Zampiron et al. 2020). However, compared to rectangular ridges, ridges with triangular cross-section induce persistent SCs at lower s/δ . In addition, the present results reveal a complex flow topology for triangular ridges in the form of additional corner vortices that appear between the lateral ridge surfaces and the flat surface sections. These corner vortices are present for all considered values of s/δ at fixed ridge width but disappear for the very wide ridge case ($b/\delta = s/\delta$). When varying ridge width at constant spacing (here $s/\delta = \pi/2$), in contrast to rectangular ridges (Hwang and Lee 2018; Medjnoun et al. 2020), the topology of the flow is not changed, i.e., no tertiary flows are formed over the tested range of ridge widths, with the widest ridge exceeding the outer scale of the flow by more than a factor of 1.5. This is attributed to the difference in ridge geometry with fewer SC-pinning corners. However, the reduction of the SCs' strength with b/δ is consistent for both shapes.

SCs induce progressively increasing levels of dispersive shear stresses as ridges are placed further apart. This trend holds until SCs reach their maximum size. Further increase in s/δ results in formation of tertiary flows and some reduction in $\langle \widetilde{uw} \rangle$. Premultiplied streamwise energy spectra were considered for different spanwise locations. Compared to the standard presentation of energy spectra, which employs spanwise averaging, significant differences between spanwise locations in terms of flow structure and energy contribution at different wavelengths are observed. In particular, the signature of SCs at high wavelength can be clearly seen in spectra sampled at the spanwise locations of secondary current centres; this signature not obvious when spectra are presented in their usual spanwise averaged form.

One of the primary findings of this study is the much stronger Reynolds number sensitivity of Reynolds and dispersive shear stresses induced by pronounced SCs than was reported previously for rectangular ridges (Vanderwel et al. 2019). Potentially, this can be attributed to the difference in the considered ridge shape, but further studies are required to discern whether sensitivity to Reynolds number is ridge shape dependent and/or affected by the flow configuration. Since secondary currents generated by ridges and those observed in non-circular ducts both represent Prandtl's secondary flows of the second kind, comparisons regarding their Reynolds number dependency can be drawn. In square ducts, secondary currents move from the duct centre closer to the corners with increasing Reynolds number until attaining a constant position (Pinelli et al. 2010). The strength of secondary currents relative to the bulk flow velocity was found for square ducts to be relatively insensitive to Reynolds number (Pirozzoli et al. 2018). In contrast, for hexagonal ducts, Marin et al. (2016) reported that with increasing Reynolds number secondary current centres move away from the duct walls, while their strength decreases. For triangular ridges, the behaviour of the wall-normal elevation of secondary currents follows a similar trend as observed in hexagonal ducts. However, an increase of the strength of secondary currents with Reynolds number was found, which is opposite to the trend observed for hexagonal ducts and instead resembles the behaviour seen in square ducts. This demonstrates that the Reynolds number dependency of Prandtl's secondary currents of the second kind is highly dependent on the particular flow configuration.

Overall, the present results show the need for further studies on ridge shapes of non-rectangular cross-section, the investigation of Reynolds number dependency of secondary currents over surfaces with streamwise aligned ridges, and the systematic comparison of secondary flows formed by identical ridge patterns but in different flow configurations.

Supplementary Information The online version contains supplementary material available at <https://doi.org/10.1007/s10494-023-00488-1>.

Author Contributions OZ: Conceptualization, Methodology, Investigation, Formal analysis, Data curation, Writing—original draft, Writing—review & editing, Visualization. TOJ: Formal analysis, Writing—review & editing. AB: Conceptualization, Methodology, Resources, Writing—review & editing, Supervision, Project administration, Funding acquisition.

Funding We gratefully acknowledge support for this work by the United Kingdom’s Engineering and Physical Sciences Research Council under grant number EP/V002066/1. This work used the ARCHER2 UK National Supercomputing Service (<https://www.archer2.ac.uk>).

Data availability The data that support the findings of this study are openly available in the University of Glasgow Enlighten repository at <https://doi.org/10.5525/gla.researchdata.1493>.

Declarations

Conflict of interest The authors have no competing interests to declare that are relevant to the content of this article.

Open Access This article is licensed under a Creative Commons Attribution 4.0 International License, which permits use, sharing, adaptation, distribution and reproduction in any medium or format, as long as you give appropriate credit to the original author(s) and the source, provide a link to the Creative Commons licence, and indicate if changes were made. The images or other third party material in this article are included in the article’s Creative Commons licence, unless indicated otherwise in a credit line to the material. If material is not included in the article’s Creative Commons licence and your intended use is not permitted by statutory regulation or exceeds the permitted use, you will need to obtain permission directly from the copyright holder. To view a copy of this licence, visit <http://creativecommons.org/licenses/by/4.0/>.

References

- Anderson, W., Barros, J.M., Christensen, K.T., et al.: Numerical and experimental study of mechanisms responsible for turbulent secondary flows in boundary layer flows over spanwise heterogeneous roughness. *J. Fluid Mech.* **768**, 316–347 (2015). <https://doi.org/10.1017/jfm.2015.91>
- Bechert, D., Bruse, M., Hage, W., et al.: Experiments on drag-reducing surfaces and their optimization with an adjustable geometry. *J. Fluid Mech.* **338**, 59–87 (1997). <https://doi.org/10.1017/S0022112096004673>
- Busse, A., Lütznier, M., Sandham, N.D.: Direct numerical simulation of turbulent flow over a rough surface based on a surface scan. *Comput. Fluids* **116**, 129–147 (2015). <https://doi.org/10.1016/j.compfluid.2015.04.008>
- Castro, I.P., Kim, J., Stroh, A., et al.: Channel flow with large longitudinal ribs. *J. Fluid Mech.* **915**, A92 (2021). <https://doi.org/10.1017/jfm.2021.110>
- Chan, L., MacDonald, M., Chung, D., et al.: Secondary motion in turbulent pipe flow with three-dimensional roughness. *J. Fluid Mech.* **854**, 5–33 (2018). <https://doi.org/10.1017/jfm.2018.570>
- Chung, D., Monty, J.P., Hutchins, N.: Similarity and structure of wall turbulence with lateral wall shear stress variations. *J. Fluid Mech.* **847**, 591–613 (2018). <https://doi.org/10.1017/jfm.2018.336>
- Endrikat, S., Modesti, D., MacDonald, M., et al.: Direct numerical simulations of turbulent flow over various riblet shapes in minimal-span channels. *Flow Turbul. Combust.* **107**(1), 1–29 (2021). <https://doi.org/10.1007/s10494-020-00224-z>
- Endrikat, S., Newton, R., Modesti, D., et al.: Reorganisation of turbulence by large and spanwise-varying riblets. *J. Fluid Mech.* **952**, A27 (2022). <https://doi.org/10.1017/jfm.2022.897>
- García-Mayoral, R., Jiménez, J.: Drag reduction by riblets. *Philos. Trans. R. Soc. A* **369**(1940), 1412–1427 (2011). <https://doi.org/10.1098/rsta.2010.0359>
- Goldstein, D., Tuan, T.C.: Secondary flow induced by riblets. *J. Fluid Mech.* **363**, 115–151 (1998). <https://doi.org/10.1017/S0022112098008921>
- Granville P (1987) Three indirect methods for the drag characterization of arbitrarily rough surfaces on flat plates. *J. Ship Res.* **31**(1)
- Gray, W.G., Lee, P.C.Y.: On the theorems for local volume averaging of multiphase systems. *Int. J. Multiph. Flow* **3**(4), 333–340 (1977). [https://doi.org/10.1016/0301-9322\(77\)90013-1](https://doi.org/10.1016/0301-9322(77)90013-1)
- Hinze, J.: Secondary currents in wall turbulence. *Phys. Fluids* **10**(9), S122–S125 (1967). <https://doi.org/10.1063/1.1762429>
- Hinze, J.O.: Experimental investigation on secondary currents in the turbulent flow through a straight conduit. *Appl. Sci. Res.* **28**, 453–465 (1973). <https://doi.org/10.1007/BF00413083>

- Hwang, H.G., Lee, J.H.: Secondary flows in turbulent boundary layers over longitudinal surface roughness. *Phys. Rev. Fluids* **3**(1), 014608 (2018). <https://doi.org/10.1103/PhysRevFluids.3.014608>
- Jiménez, J., Pinelli, A.: The autonomous cycle of near-wall turbulence. *J. Fluid Mech.* **389**, 335–359 (1999). <https://doi.org/10.1017/S0022112099005066>
- Kevin, K., Monty, J.P., Bai, H., et al.: Cross-stream stereoscopic particle image velocimetry of a modified turbulent boundary layer over directional surface pattern. *J. Fluid Mech.* **813**, 412–435 (2017). <https://doi.org/10.1017/jfm.2016.879>
- Lee, M., Moser, R.D.: Direct numerical simulation of turbulent channel flow up to $Re_\tau \approx 5200$. *J. Fluid Mech.* **774**, 395–415 (2015). <https://doi.org/10.1017/jfm.2015.268>
- Liu, Y., Stoesser, T., Fang, H.: Effect of secondary currents on the flow and turbulence in partially filled pipes. *J. Fluid Mech.* **938**, A16 (2022). <https://doi.org/10.1017/jfm.2022.141>
- Marin, O., Vinuesa, R., Obabko, A., et al.: Characterization of the secondary flow in hexagonal ducts. *Phys. Fluids* (2016). <https://doi.org/10.1063/1.4968844>
- Medjnoun, T., Vanderwel, C., Ganapathisubramani, B.: Effects of heterogeneous surface geometry on secondary flows in turbulent boundary layers. *J. Fluid Mech.* **886**, A31 (2020). <https://doi.org/10.1017/jfm.2019.1014>
- Medjnoun, T., Rodriguez-Lopez, E., Ferreira, M.A., et al.: Turbulent boundary-layer flow over regular multi-scale roughness. *J. Fluid Mech.* **917**, A1 (2021). <https://doi.org/10.1017/jfm.2021.228>
- Monty, J., Hutchins, N., Ng, H., et al.: A comparison of turbulent pipe, channel and boundary layer flows. *J. Fluid Mech.* **632**, 431–442 (2009). <https://doi.org/10.1017/S0022112009007423>
- Nikuradse, J.: Untersuchungen über turbulente Strömungen in nicht kreisförmigen Röhren. *Ingenieur-Archiv* **1**, 306–332 (1930). <https://doi.org/10.1007/BF02079937>
- Pinelli, A., Uhlmann, M., Sekimoto, A., et al.: Reynolds number dependence of mean flow structure in square duct turbulence. *J. Fluid Mech.* **644**, 107–122 (2010). <https://doi.org/10.1017/S0022112009992242>
- Pirozzoli, S., Modesti, D., Orlandi, P., et al.: Turbulence and secondary motions in square duct flow. *J. Fluid Mech.* **840**, 631–655 (2018). <https://doi.org/10.1017/jfm.2018.66>
- Prandtl, L.: *Essentials of Fluid Dynamics: With Applications to Hydraulics, Aeronautics, Meteorology, and Other Subjects*. Blackie (1952)
- Raupach, M.R., Shaw, R.H.: Averaging procedures for flow within vegetation canopies. *Bound. Layer Meteorol.* **22**(1), 79–90 (1982). <https://doi.org/10.1007/BF00128057>
- Stroh, A., Hasegawa, Y., Kriegseis, J., et al.: Secondary vortices over surfaces with spanwise varying drag. *J. Turbul.* **17**(12), 1142–1158 (2016). <https://doi.org/10.1080/14685248.2016.1235277>
- Stroh, A., Schäfer, K., Foroughi, P., et al.: Secondary flow and heat transfer in turbulent flow over streamwise ridges. *Int. J. Heat Fluid Flow* **81**(108), 518 (2020). <https://doi.org/10.1016/j.ijheatfluidflow.2019.108518>
- Stroh, A., Schäfer, K., Frohnäpfel, B., et al.: Rearrangement of secondary flow over spanwise heterogeneous roughness. *J. Fluid Mech.* **885**, R5 (2020). <https://doi.org/10.1017/jfm.2019.1030>
- Vanderwel, C., Ganapathisubramani, B.: Effects of spanwise spacing on large-scale secondary flows in rough-wall turbulent boundary layers. *J. Fluid Mech.* **774**, R2 (2015). <https://doi.org/10.1017/jfm.2015.292>
- Vanderwel, C., Stroh, A., Kriegseis, J., et al.: The instantaneous structure of secondary flows in turbulent boundary layers. *J. Fluid Mech.* **862**, 845–870 (2019). <https://doi.org/10.1017/jfm.2018.955>
- von Deyn, L.H., Gatti, D., Frohnäpfel, B., et al.: Parametric study on ridges inducing secondary motions in turbulent channel flow. *PAMM* **20**(1), e202000139 (2021). <https://doi.org/10.1002/pamm.202000139>
- Von Deyn, L.H., Gatti, D., Frohnäpfel, B.: From drag-reducing riblets to drag-increasing ridges. *J. Fluid Mech.* **951**, A16 (2022). <https://doi.org/10.1017/jfm.2022.796>
- von Deyn, L.H., Schmidt, M., Örlü, R., et al.: Ridge-type roughness: from turbulent channel flow to internal combustion engine. *Exp. Fluids* **63**(1), 18 (2022). <https://doi.org/10.1007/s00348-021-03353-x>
- Wang, Z.Q., Cheng, N.S.: Time-mean structure of secondary flows in open channel with longitudinal bedforms. *Adv. Water Resour.* **29**(11), 1634–1649 (2006). <https://doi.org/10.1016/j.advwatres.2005.12.002>
- Wangsawijaya, D.D., Baidya, R., Chung, D., et al.: The effect of spanwise wavelength of surface heterogeneity on turbulent secondary flows. *J. Fluid Mech.* **894**, A7 (2020). <https://doi.org/10.1017/jfm.2020.262>
- Yang, J., Anderson, W.: Numerical study of turbulent channel flow over surfaces with variable spanwise heterogeneities: topographically-driven secondary flows affect outer-layer similarity of turbulent length scales. *Flow Turbul. Combust.* **100**, 1–17 (2018). <https://doi.org/10.1007/s10494-017-9839-5>
- Yang, J., Balaras, E.: An embedded-boundary formulation for large-eddy simulation of turbulent flows interacting with moving boundaries. *J. Comput. Phys.* **215**(1), 12–40 (2006). <https://doi.org/10.1016/j.jcp.2005.10.035>
- Zampiron, A., Cameron, S., Nikora, V.: Secondary currents and very-large-scale motions in open-channel flow over streamwise ridges. *J. Fluid Mech.* **887**, A17 (2020). <https://doi.org/10.1017/jfm.2020.8>
- Zhou, J., Adrian, R.J., Balachandar, S., et al.: Mechanisms for generating coherent packets of hairpin vortices in channel flow. *J. Fluid Mech.* **387**, 353–396 (1999). <https://doi.org/10.1017/S002211209900467X>